

See discussions, stats, and author profiles for this publication at: <https://www.researchgate.net/publication/304106132>

# The effects of high frequency current ripple on electric vehicle battery performance

Article in *Applied Energy* · September 2016

DOI: 10.1016/j.apenergy.2016.06.033

CITATIONS

160

READS

4,074

4 authors, including:



**Kotub Uddin**

OVO Energy

34 PUBLICATIONS 2,462 CITATIONS

[SEE PROFILE](#)



**Andrew Moore**

The University of Warwick

11 PUBLICATIONS 435 CITATIONS

[SEE PROFILE](#)

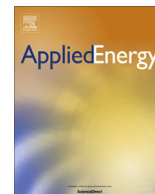


**Anup Barai**

The University of Warwick

53 PUBLICATIONS 1,760 CITATIONS

[SEE PROFILE](#)



# The effects of high frequency current ripple on electric vehicle battery performance



Kotub Uddin<sup>\*</sup>, Andrew D. Moore, Anup Barai, James Marco

WMG, International Digital Laboratory, The University of Warwick, Coventry CV4 7AL, UK

## HIGHLIGHTS

- Experimental study into the impact of current ripple on li-ion battery degradation.
- 15 cells exercised with 1200 cycles coupled AC–DC signals, at 5 frequencies.
- Results highlight a greater spread of degradation for cells exposed to AC excitation.
- Implications for BMS control, thermal management and system integration.

## ARTICLE INFO

### Article history:

Received 8 April 2016

Received in revised form 19 May 2016

Accepted 11 June 2016

Available online 17 June 2016

### Keywords:

Hybrid electric vehicle (HEV)

Electric vehicle (EV)

Battery management system (BMS)

Li-ion cell

Battery degradation

Ageing

Current ripple

## ABSTRACT

The power electronic subsystems within electric vehicle (EV) powertrains are required to manage both the energy flows within the vehicle and the delivery of torque by the electrical machine. Such systems are known to generate undesired electrical noise on the high voltage bus. High frequency current oscillations, or ripple, if unhindered will enter the vehicle's battery system. Real-world measurements of the current on the high voltage bus of a series hybrid electric vehicle (HEV) show that significant current perturbations ranging from 10 Hz to in excess of 10 kHz are present. Little is reported within the academic literature about the potential impact on battery system performance and the rate of degradation associated with exposing the battery to coupled direct current (DC) and alternating currents (AC). This paper documents an experimental investigation that studies the long-term impact of current ripple on battery performance degradation. Initial results highlight that both capacity fade and impedance rise progressively increase as the frequency of the superimposed AC current increases. A further conclusion is that the spread of degradation for cells cycled with a coupled AC–DC signal is considerably more than for cells exercised with a traditional DC waveform. The underlying causality for this degradation is not yet understood. However, this has important implications for the battery management system (BMS). Increased variations in cell capacity and impedance will cause differential current flows and heat generation within the battery pack that if not properly managed will further reduce battery life and degrade the operation of the vehicle.

© 2016 The Authors. Published by Elsevier Ltd. This is an open access article under the CC BY-NC-ND license (<http://creativecommons.org/licenses/by-nc-nd/4.0/>).

## 1. Introduction

Within the automotive and road transport sector, one of the main drivers for technological development and innovation is the need to reduce the vehicle's fuel consumption and the emissions of carbon dioxide (CO<sub>2</sub>) [1–3]. Legislative requirements are motivating manufacturers and subsystem suppliers to develop new and innovative technologies for low carbon mobility [4–7]. In conventional vehicles, lightweight materials [8] and advanced combustion engines [9] are continually being improved to increase

fuel economy. Concurrently, much attention is being diverted to vehicle electrification as battery technologies become more accessible [10]. Although electric vehicles (EV), hybrid electric vehicles (HEV) and plug-in hybrid electric vehicles (PHEV) remain a small fraction of the market today, electrified powertrains are expected to become ubiquitous by 2030 [11,12]. Within this field, a key enabling technology is the design and integration of the power electronic subsystems that are required to manage the flow of energy within the vehicle and the creation of torque by the electrical machine during vehicle acceleration and regenerative braking. A comprehensive review of different hybrid powertrain architectures employed in commercial vehicles with detailed descriptions of power electronic components can be found in Ref. [13]. Such

<sup>\*</sup> Corresponding author.

E-mail address: [k.uddin@warwick.ac.uk](mailto:k.uddin@warwick.ac.uk) (K. Uddin).

## Nomenclature

### Terms and abbreviations

AC	alternating current
BMS	battery management system
CC	constant current
CV	constant voltage
DC	direct current
DOD	depth of discharge
EV	electric vehicle
EIS	electrochemical impedance spectroscopy
EMF	electromotive force
FET	field effect transistors
HEV	hybrid electric vehicle
ICE	internal combustion engine
IGBT	insulated gate bipolar transistor
Li	lithium

MOSFET	metal–oxide–semiconductor field-effect transistor
Pb	lead
PHEV	plug-in hybrid electric vehicle
SEI	solid electrode interface
SOC	state of charge

### Mathematical notation

$C_{dl}$	double layer capacitance (F)
$I_{DC}$	DC current value (A)
$f_c$	critical frequency (Hz)
$f$	frequency (Hz)
$R_{ct}$	charge transfer resistance ( $\Omega$ )
$R_0$	ohmic resistance ( $\Omega$ )
$X_{ct}$	reactance ( $\Omega$ )

electrified powertrains typically contain modern electronic switching circuits and power electronic components such as Insulated Gate Bipolar Transistors (IGBT) and Field Effect Transistors (FET) integrated within both DC–DC bi-directional converters and electrical machine inverter drives [14] and can operate at switching frequencies in the order 20 kHz – 50 kHz within a vehicle application [15]. This switching operation coupled with the highly reactive load associated with the vehicle's electrical machine is known to induce higher frequency harmonic signals that are coupled with the DC battery current [16]. The rechargeable battery employed within both EV and HEVs is often characterised as having a useful life defined by the number of continuous charge–discharge cycles with respect to a given level of capacity fade [17]. For example, the 40 Ah nickel manganese cobalt oxide battery produced by Dow Kokam designed for automotive applications is cited by [18] as having a retained capacity of 89.5% after 1900 cycles at a current rate of 1C and temperature of 25 °C. Within each cycle the coulombic capacity of the battery is generally known to reduce [19,20]. It follows that low coulomb charge–discharge cycles at high frequencies may also have a detrimental effect on useful battery life. Alternating currents (AC), in essence, produce repeated coulomb charge–discharge cycles that may affect the life of the battery. As defined through electrochemical impedance spectroscopy (EIS) techniques both the reactive and ohmic components of the cell's impedance vary as a function frequency, implying that any effect may equally be dependent on the frequency and magnitude of the applied current.

Little is reported within the academic literature about the potential impact on battery system performance and the rate of degradation associated with exposing the battery to coupled direct current (DC) and AC excitation. Many early laboratory and real world studies of lead acid (Pb) batteries have shown that AC ripple may cause the cell to experience shallow discharge cycles, that in turn may lead to gassing [21], grid corrosion [22–24] and internal heat generation [21,22,25,26]. All factors that have a well understood detrimental impact on the service life of lead acid batteries [27]. In addition, for a fully charged lead–acid battery, high-frequency ripple can be destructive through overcharge, especially due the large differences in electrochemical efficiency for charge and discharge [21]. More recently, Uno and Tanaka [28] have studied the lifetime performance of Lithium-ion batteries (2 Ah prismatic Sanyo battery with a  $\text{LiCoO}_2$  positive electrode and a graphite negative electrode) when subject to AC ripple excitation at frequencies ranging from 1 Hz – 100 kHz. The authors employed a single AC current waveform (of a single frequency) with peak-to-peak current of 2 A with no DC offset (e.g. zero mean) as the excitation signal. This means that the tests were carried out

around a single SOC operating and therefore at a single voltage point. The reference cell against which comparisons of performance degradation were made was a single cell, under no-load, stored within the same environmental conditions. It was shown that cells cycled at frequencies above 10 Hz showed trends in performance degradation commensurate with calendar aging. Conversely, the performance of cells cycled using a low frequency current waveform (below 10 Hz) significantly deteriorated. A capacity fade in the order of 14% was noted for the latter test condition.

Though not experientially substantiated, this has often been attributed to the time constant associated with the double-layer capacitance ( $C_{dl}$ ) and charge-transfer resistance ( $R_{ct}$ ) found in both the anode and the cathode. When the time period of the high-frequency cycles are significantly shorter than the  $R_{ct}C_{dl}$  time constant, the relatively slow charge transfer dynamics of the cell does not have time to respond to the current perturbation [21,25]. This hypothesis is consistent with previous studies into lead–acid batteries that conclude that high-frequency current fluctuations only charge and discharge the double-layer capacitance and do not allow time for a significant amount of ionic diffusion to occur. Conversely, ionic diffusion in the solid phase is fully operative at lower frequencies (below < 1 Hz [29]).

Simulation analysis reported within [28] using an equivalent circuit model (ECM – with two RC branches approximating the dynamics of each electrode) show little current flowing through the charge-transfer resistor  $R_{ct}$  at high frequencies (above 100 Hz). These results are further employed to argue that at high frequencies the charge–discharge current is effectively “buffered” since the majority of current will flow through the lower capacitive reactance of  $X_{ct}$ .

$$X_{ct} = \frac{1}{2\pi f C_{dl}} \quad (1)$$

Conversely, the current through  $R_{ct}$  will dominate heat generation at low frequencies. The internal heating of lithium-ion batteries with very low frequency (< 1 Hz) sinusoidal alternating currents is documented in Ref. [30]. A correlation identified between the degradation trend and the current distribution of  $C_{dl}$  and  $R_{ct}$  additionally indicates that significant degradation at low frequencies is caused by side reactions that accompany the charge-transfer process [28]. At high frequencies, it is argued that ripple current only acts to cycle the energy throughput of  $C_{dl}$  and therefore cell degradation mimics calendar degradation. While the conclusions made are consistent with those reported in similar studies, it is noteworthy that these conclusions are based on simulation results obtained through the use of an ECM. This represen-

tation of the cell, inherently lacks the fidelity, most noticeably the ability to define the electrochemical causality within the cell to accurately predict the effect of AC current ripple.

Previous research into cycle life ageing of lithium ion batteries have either considered degradation arising from direct current loads only [31–33] or alternating current loads only [28]. These signals do not accurately reflect the load current within the context of real-life battery operation which involves a coupling between AC and DC which is arguably more valuable to the engineering community to understand. In this work therefore we carry out novel research into long-term performance degradation of li-ion battery cells when exposed to a coupled AC–DC current waveform that is representative of real-world HEV use. In this work, we quantify battery degradation caused by a coupled AC–DC excitation, which is designed from measurements of current on the high voltage bus of a HEV, within a temperature controlled environment.

This paper is structured as follows: measurements of high frequency ripple on the DC link of a series hybrid electric vehicle are presented in Section 2. To generate a coupled AC–DC signal, a bespoke test rig was created; the details of this new test environment along with the experimental method employed are explained in Section 3. Within Section 4, the test procedure including the characterisation method is presented. Experimental results, discussion and conclusions are provided in Sections 5, 6 and 7 respectively.

## 2. Measurement of electrical noise on the DC link of the high voltage bus

In this work we consider a series HEV powertrain where the vehicle's high voltage battery system is connected electrically in series with the electrical machine used for vehicle propulsion. An example configuration is illustrated in Fig. 1. The figure highlights the inclusion of the different power electronic subsystems used within the vehicle. These include the DC–DC bidirectional converter, employed to step-up the voltage of the battery pack to that employed on the high voltage bus or DC link. The AC–DC converter (rectifier) employed to integrate the internal combustion engine (ICE) with the electrical architecture of the vehicle and finally the DC–AC converter (inverter) used to regulate the current and therefore the torque output of the electrical machine. It is beyond the scope of this paper to discuss, in detail, the characteristics of each subsystem. Their operation, within the context of new automotive applications, is documented within a number of educational text and research papers including [34].

Within an electrified powertrain AC signals are generated within the electrical architecture by the power electronic subsystems. The continual switching of the IGBTs or MOSFETs embedded within their designs generate electrical noise at their respective switching frequency and multiples of the switching frequency thereafter (e.g. including even or odd harmonics from

non-sinusoidal waveforms). This higher frequency content is often filtered through a low-pass filter integrated within the output stage of the power electronics before passing through to the DC link. However, while it may be attenuated, it is not completely eliminated. For a typical vehicle application, the DC–AC inverter is responsible for producing AC waveforms typically in the order of 8–10 kHz limited by the maximum switching frequency of the power electronics and any DC–DC converter in the system (30–50 kHz). If the vehicle has the ability to integrate with the electrical grid, then the associated charger circuits will induce further electrical interference in the order of twice the grid frequency due to full wave rectification.

Another source of high frequency AC ripple on the DC link, is from the electrical machine employed for vehicle propulsion. The machine produces odd harmonics arising from the non-sinusoidal back-EMF (electromagnetic force) waveform. The machine produces even harmonics arising from changes in the mutual inductance of the windings as the rotor moves within the magnetic field established by the excitation currents. This higher frequency content manifest itself at even harmonic values of the rotational frequency due to the equal number of pole-pairs in the machine design. A further source of high frequency ripple within the electrical machine stems from subtle differences in the winding impedance that can be found in each of the machine's phases. For a three phase machine, in an ideal scenario the current through each phase (separated 120° electrically), will sum vectorially to zero. However, small differences in impedance for each phase will result in differential current flowing through each phase that will not, as a result, resolve to zero and hence generate AC ripple on the DC link. This high frequency content manifests itself at odd harmonic values of the fundamental motor excitation frequency.

In order to quantify the frequency content of the load current on the DC link of an actual HEV, a sample of the DC–link current was measured under a transient load conditions for a commercially available PHEV during a regenerative braking manoeuvre. This waveform was sampled at a frequency of 10<sup>9</sup> Hz to ensure the bandwidth of the dataset was appropriate for this analysis. This data was converted into the frequency domain using Welch's method [35] available as a toolbox within the commercially available Matlab software. This technique estimates the power content of the signal at difference frequencies and its use is widely reported [36]. The output from this algorithm is summarised in Table 1 and presented graphically in Fig. 2.

## 3. Design of the bespoke AC ripple testing rig and the experimental set-up

### 3.1. Description of the test cells

Within this study, 15 commercially available 3 Ah 18650 cells were used. Each cell comprises of a LiC<sub>6</sub> negative electrode,

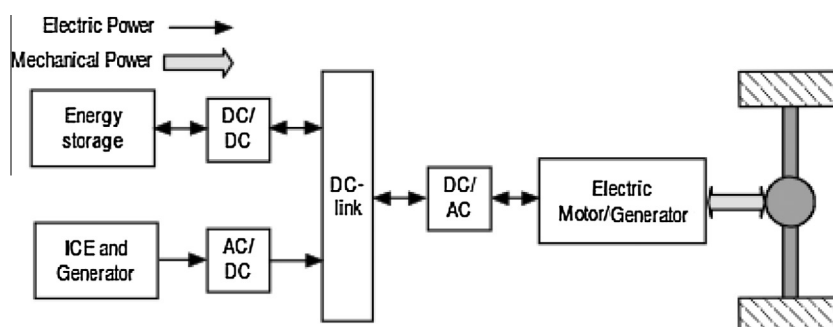


Fig. 1. Typical series hybrid electric vehicle (HEV) powertrain configuration.

**Table 1**

A summary of spectral analysis results.

Frequency (Hz)	Power/frequency (dB/Hz)
0.15	101
53	57.17
106	67.34
255	48.8
361	35.13
510	30.81
1020	12.54
1529	17.29
2549	13.2
5704	2.9
9890	0.3539
14,828	−2.498
49,119	7.119
82,460	−6.02

LiNiCoAlO<sub>2</sub> positive electrode, separated by a polyethylene separator, sandwiched between two current collectors and immersed in an electrolyte solution. The manufacturers recommended maximum continuous charge and discharge current rates are defined as 1.2C and 0.3C respectively. The maximum instantaneous charge and discharge current rates are defined as 5C and 1.5C respectively. Fig. 3 presents one EIS plot for a cell under test, with a stored energy of 50% SOC measured at ambient temperature (25 °C). To further contextualise the research problem and to correlate the cell's impedance characteristics to the application domain introduced in Section 2, a subset of pertinent frequency points are highlighted. Two further points are also defined, namely the impedance when  $Im(Z(f)) = 0$  the pure Ohmic resistance of the battery ( $R_0$ ) and the real part of the battery impedance at the point where the negative imaginary part has its local minimum ( $R_t$ ). The latter corresponding to the sum of  $R_0$  and  $R_{ct}$ . The value of  $R_t$  is often employed as a measure of the power capability of the battery

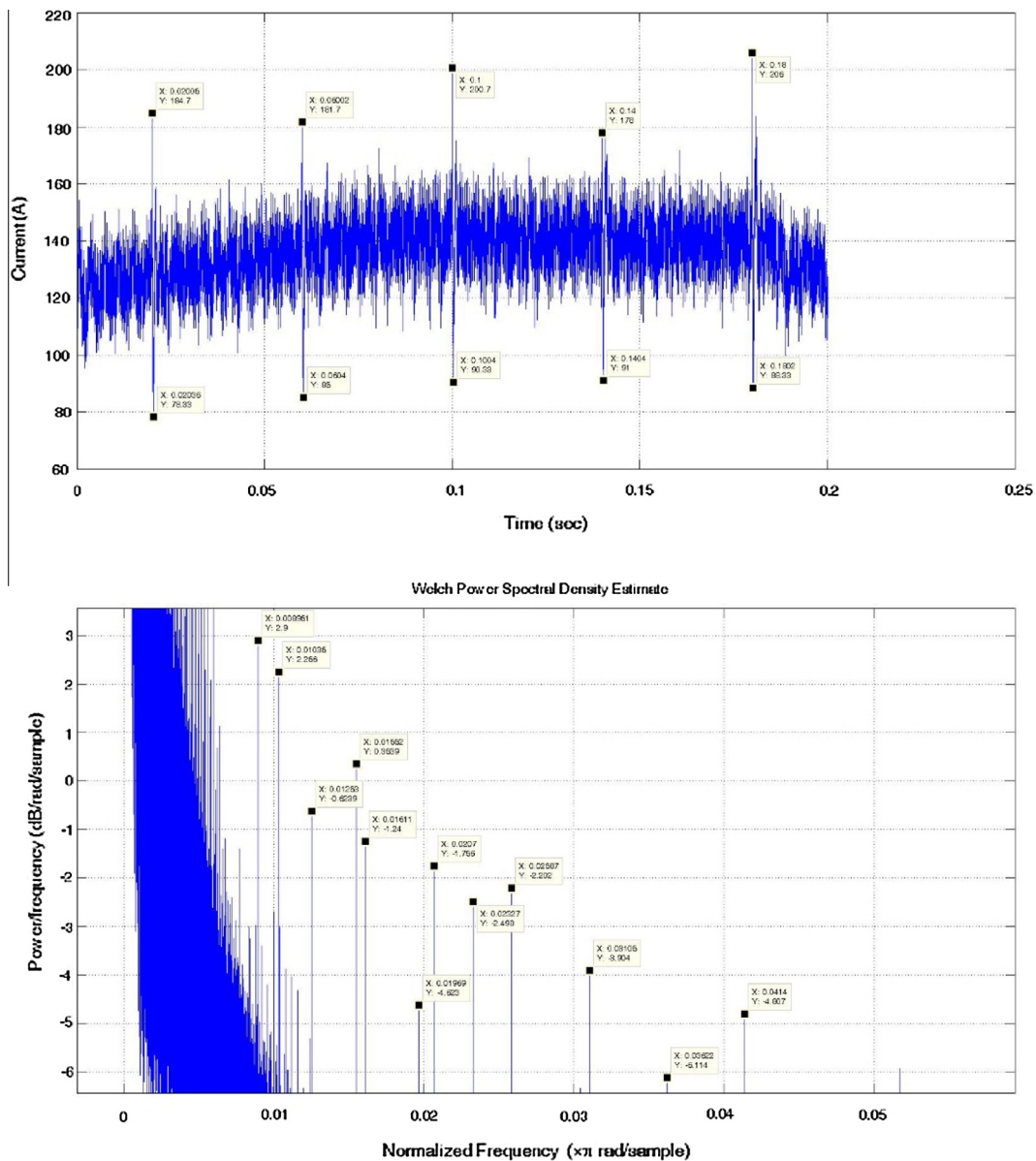


**Fig. 2.** Top panels shows a high resolution measurement (nano-seconds) of current (y-axis) on the DC link of a typical series hybrid electric vehicle during a braking event. The bottom panel shows a small sample of the power spectrum; the y-axis is normalised power (dB/ $\pi$ /sample frequency (Hz)) and the x-axis is normalised frequency ( $\pi$ /sample frequency (Hz)).



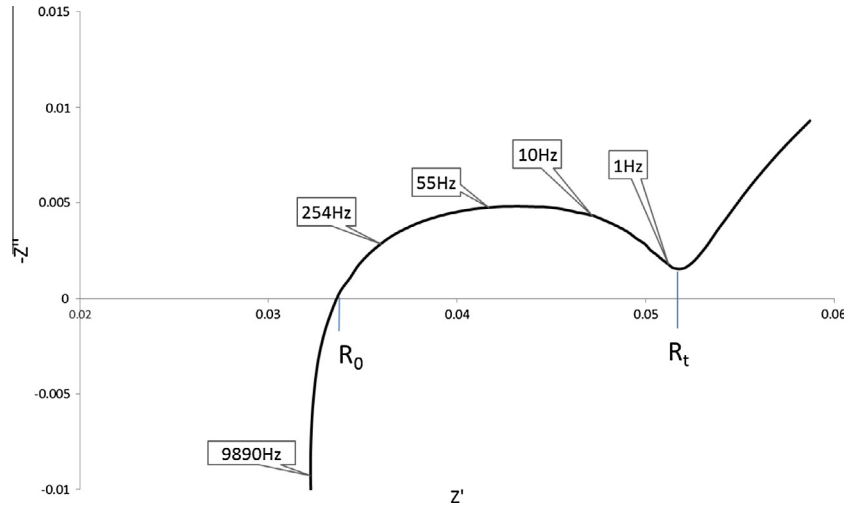


Fig. 3. EIS results for the 3 Ah 18,650 cell showing selected frequencies measured on the high voltage bus during a regenerative braking event.

system [18] or the effective resistance of the battery measured by the BMS at a measurement sample rate of 0.1 Hz – 1 Hz [37]. Also highlighted on the EIS plot is the characteristic frequency ( $f_c$ ) of the cell, measured at the point where the vector ( $\frac{1}{RC}$ ) is at a maximum. The characteristic frequency defines the voltage response dynamics of the battery. From Fig. 3, it can be seen that 55 Hz is very close to the characteristic frequency for this cell. Based on previous research [28], it is assumed therefore that electrical loading of the cell below 55 Hz will cycle the SOC of the cell leading in the longer term to performance degradation. Based on the results presented in Fig. 3 and the discussion provided in Section 2, five different excitation signals are defined to electrically load the different cells. These are:

- An electrical AC signal at 55 Hz superimposed onto a DC signal ( $f = f_c$ )
- An electrical AC signal at 10 Hz superimposed onto a DC signal ( $f < f_c$ )
- An electrical AC signal at 254 Hz superimposed onto a DC signal ( $f > f_c$ )
- An electrical AC signal at 14.8 kHz superimposed onto a DC signal ( $f \gg f_c$ ) to emulate the high frequency harmonic content entering the traction battery.
- A pure DC signal to act as both the reference condition and to emulate the traditional model of electrical loading the battery cell within a HEV test scenario or battery ageing study.

To improve the robustness of the test method and the efficacy of the conclusions made, 3 cells of the same type and are exercised using each current waveform defined above.

### 3.2. Test cycle definition

Each cell is cycled using a DC current signal superimposed with the AC ripple current waveform. Each cell is discharged using one of the five current waveforms defined in Section 3.1 with a DC of  $0.8C_{cycle}$  (where  $C_{cycle}$  is the de-rated battery C-rate defined after each characterisation test) from 95%  $SOC_{cycle}$  to 65%  $SOC_{cycle}$ . Following a rest period of 10 min, each cell is then charged using a standard constant current (CC) – constant voltage (CV) strategy. The cells are charged with a DC rate of  $0.3 C_{cycle}$  from 65%  $SOC_{cycle}$  until the upper voltage limit of 4.1 V (corresponding to 95%  $SOC_{cycle}$ ) is reached. Each cell is then charged under CV conditions using a simple DC current waveform, until the magnitude of the applied

current reduces below a threshold of 0.15 A. The DC portion of the testing is based on the battery specification presented in Section 3.1, the following constraints were derived to ensure the safe operation of the experimental activity:

- Condition 1:  $I \equiv I_{DC} + |I_{AC}| \sin(2\pi ft) < 1.5C(I_{DC} \leq 0.3C)$  during charge
- Condition 2:  $I \equiv I_{DC} + |I_{AC}| \sin(2\pi ft) > -5C(I_{DC} \geq -1.2C)$  during discharge
- Condition 3:  $ft_{charge} = 2\pi n_{charge}$  during charge
- Condition 4:  $ft_{discharge} = 2\pi n_{discharge}$  during discharge
- Condition 5:  $|I_{AC}| = 0$  during constant voltage charging phase

$I_{DC}$  is the magnitude of the DC current (A),  $|I_{AC}|$  is the magnitude of the AC signal (A),  $f$  is frequency (Hz),  $t$  is time (s),  $n_{charge}$  and  $n_{discharge}$  is the number of complete AC periods within each charge and discharge mode respectively. Conditions 1 and 2 ensure that current during the test does not exceed the manufacturer's recommended limits for the current rating. Conditions 3 and 4, ensure that the average energy throughput for each cell, irrespective of the frequency of the applied current waveform is equal to:

$$\int I_{DC} dt \quad (2)$$

over the complete charge–discharge cycle. While violating Conditions 3 and 4 for higher frequency current signals may result in negligible amounts of differential energy being sunk and/or sourced from each cell; for the lower frequency test signals, the cumulative energy content contained within part of the period, may be significant. Given that the primary focus of this research is to better understand the potential impact of AC current ripple on battery performance, the magnitude of the sinusoidal current element of the excitation signal is fixed to 1.2 C peak-to-peak so that a significant contribution of the total applied current is alternating. Applying Conditions 1 and 2, the DC part of the test signal is summarised in Table 2. It is noteworthy that current magnitudes defined in the table are expressed relative to the de-rated capacity of each cell ( $C_{cycle}$ ), the value of which was repeatedly measured at ageing characterisation points after 300, 600, 900 and 1200 complete charge–discharge cycles. Using  $C_{cycle}$  accounts for capacity fade during the test and ensure that the safe operating limits expressed by the manufacturer are adhered too. For completeness, an example illustration of the current profile that will be used to cycle the cells

**Table 2**

Definition of the DC part of the cycle, where  $C_{\text{cycle}}$  is the de-rated ampere-hour rating of the cell (updated after each characterisation test) and  $\text{SOC}_{\text{cycle}}$  is the state of charge defined using  $C_{\text{cycle}}$ .

Mode	Description	Time
Discharge	$0.8C_{\text{cycle}}$ discharge from 95% $\text{SOC}_{\text{cycle}}$ to 65% $\text{SOC}_{\text{cycle}}$	22.5 min
Rest	No current	10 min
Charge	$0.3C_{\text{cycle}}$ charge from 65% $\text{SOC}_{\text{cycle}}$ until 4.1 V (95% $\text{SOC}_{\text{cycle}}$ ) is reached or until the current falls below 0.15 A	~60 min
Rest	No current	10 min

( $f = 0.006$  Hz) is shown in Fig. 4. The total elapsed time to complete one charge–discharge cycle is approximately 100 min.

### 3.3. Description of the bespoke amplifier circuit design

A high level representation of the experimental setup is presented in Fig. 5. The equipment employed comprises of a bespoke

amplifier to generate the AC waveform, a Bitrode cell cycler (with associated monitoring and control software) to generate the DC load profile, a Tektronix non-contact current probe and oscilloscope, the battery cells under test, an AC coupling capacitance between the amplifier output and the cells and finally, a thermal management rig to ensure that ambient temperature is maintained at 25 °C. As discussed below, the thermal management solution adapted the use of a commercially available LAUDA (Model Proline RP845C) heating and cooling unit to achieve the desired function. Table 3 summarises the pertinent measurement and accuracy characteristics associated with the equipment employed.

The primary requirement for the test environment is to exercise each cell with a defined DC charge–discharge cycle that includes the superposition of a stable and known AC ripple current waveform. To better understand the effects of specific frequencies on battery performance and degradation, the excitation signal should not contain any parasitic harmonics. For this reason, a bespoke amplifier circuit was designed and commissioned for this research.

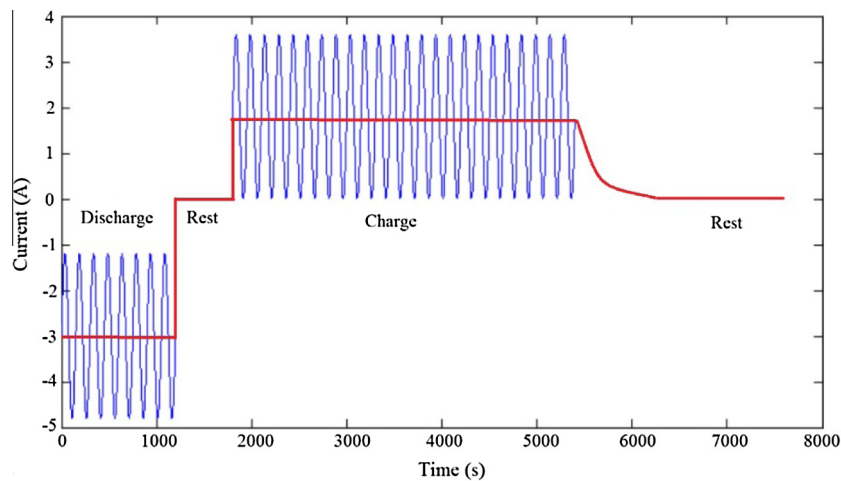


**Fig. 4.** Example test signal as described in Section 3.3, showing a DC signal with a superimposed AC cycle (for illustrative purposes).

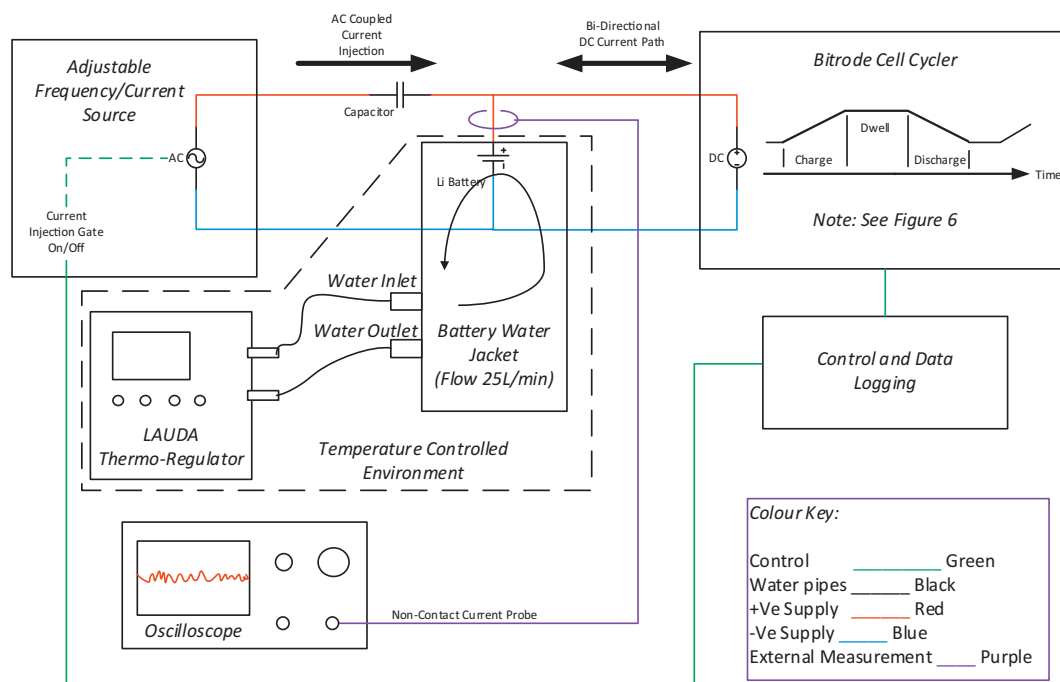


**Fig. 5.** High level experimental set-up.

**Table 3**

Table listing key test components with values, range, resolution and accuracy.

Component	Values	Measurement range	Resolution	Accuracy (FSD)
Adjustable frequency current source	As results	10 – 20 kHz	9 bit	±2%
Oscilloscope + current probe	n/a	0 – 20 A	9 bit	±2%
Lauda thermo-regulator	25 L/min	0 – 25 L/min	±0.01 °C	±0.1%
Bitrode cell cyclers output	Fig. 6	0 – 5 V	16 bit	±0.1%
Bitrode cell cyclers current measure	Fig. 6	0 – 100 A	16 bit	±0.1%
Bitrode cell cyclers voltage measure	Fig. 6	0 – 5 V	16 bit	±0.1%
Capacitor	1000 µF	n/a	n/a	n/a
Data logging	PC	n/a	n/a	n/a

A detailed discussion into the design of the amplifier is beyond the scope of this paper and will be the subject of another publication. Key characteristics, pertinent to this research are discussed below for completeness.

A class-AB amplifier architecture was employed. The amplifier provides a harmonic distortion of less than  $\pm 0.03$ . The amplifier was designed to have a constant gain of 0 dB from zero hertz to the bandwidth frequency of 20 kHz. The amplifier essentially constitutes a high accuracy voltage controlled AC current source. The Bitrode cell cyclers (employed to generate  $I_{DC}$ ) have the negative voltage terminal above the ground plane. As a result, it was necessary to provide a floating voltage output for the amplifier to prevent the circulation of parasitic currents (earth-loops) producing current generation errors.

As shown in Fig. 5, the output from the amplifier is capacitively coupled to the positive terminal of the cells under test and the local isolated return path of the amplifier is connected to the battery's negative terminal. The output from the battery cycler (positive and negative terminals) are connected to the battery to provide the DC charging and discharging profile. The oscilloscope's isolated current probe is connected to the battery positive terminal to measure the AC ripple component added to the DC waveform. The AC ripple current can be turned on and off as required by the control system, which also monitors and controls the DC charging bias from the Bitrode cell cycler. The control system ensures that the AC ripple current is only applied to the cell during the charge (CC) and discharge phases of the complete cycle and isolated from the cells during the rest periods and during CV charging.

The Bitrode control programme provides the main charge-dwell-discharge profile at the specified C-rate to the cells under test using only a single DC return path. This single DC path is ensured by the electrical isolation provided by the amplifier. Any DC component present at the amplifier output stage is reduced to a negligible level by the introduction of the AC coupling capacitor connected between the amplifier output and the positive terminal of the battery. The amplifier introduced DC component is limited to only capacitor leakage currents that were measured to be in the order of 100 µA. Thus at 2.4 A the additional DC current results in an error of less than 1 part in 24,000. A value that is well within the measurement resolution of the Bitrode unit and therefore ignored. In addition to the control of the DC load current, the Bitrode unit also provides data logging (current and voltage) at a sample rate of 10 Hz with a 16 bit measurement resolution of current and voltage (1.5 mA and 76 µV respectively).

The AC current component measured using the Oscilloscope (Tektronix TCP312) with the non-contact probe and probe amplifier (TCP300A) were calibration validated in combination to provide C-rate resolution to  $\pm 2\%$  of the actual current value and  $10^{-6}\%$  of the measured frequency. The ripple amplitude and frequency present on the cell when measured at intervals over the period of the test, was stable to within the  $\pm 1\%$  of amplitude and  $10^{-6}\%$  of frequency.

The temperature stability of the cells under test was ensured by embedding the cells within a temperature controlled environment in which the ambient temperature was controlled using a commercially available LAUDA (Proline RP845C) unit. This thermo-regulator unit provides 0.01 °C resolution for the control temperature. Short term fluctuations in the temperature of each cell was minimised through conduction, in which water at a high flow rate (circa: 25 L/min), was passed through a cooling jacket in contact with the radial surface of each cell. The temperature at the water cooled cell jacket was measured at the inlet to the LAUDA unit and was found to be stable to  $25 \pm 0.5$  °C.

#### 4. Experimental procedure

The high level experimental procedure followed for this research is presented in Fig. 6.

##### 4.1. Initial characterisation test

In order to determine and quantify the performance degradation caused by electrically cycling the cells with a coupled DC and AC test signal, it is first necessary to characterise each cell. Standard methods employed within the energy storage research community were employed and include for each cell:

- A measurement of open circuit voltage at ambient temperature (25 °C)
- A retained capacity measurement at a temperature of 25 °C for a constant discharge current of 1C, C/10 and C/25 respectively.
- The use of power pulse tests to estimate the resistance of each cell, in which the voltage response of each cell is measured for a 10 s current pulse at 20%, 40%, 60%, 80% and 100% of the manufacturers recommended maximum continuous charge and discharge current. Pulses are applied to each cell when preconditioned to a SOC of 90%, 50% and 20% respectively, with all tests conducted at an ambient temperature of 25 °C.
- The measurement of the cells impedance through EIS, with the cells preconditioned to a SOC of 90%, 50% and 20% respectively. All tests were conducted at an ambient temperature of 25 °C.

A detailed description of each characterisation stage, including the relative accuracy of the test and the times allowed for the cells to equilibrate between changes of SOC and temperature are described fully within [38–40] and therefore will not be repeated here.

##### 4.2. The AC ripple test

Each cell was allocated a unique number ranging from 1 to 15 and exercised using the coupled AC–DC waveforms described in Section 3.1 and presented graphically in Fig. 4. Cells 1–3 were



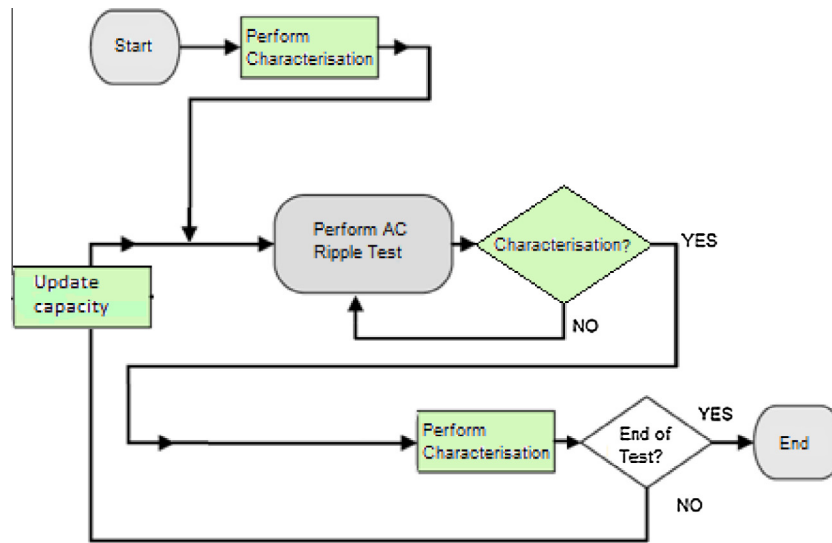


Fig. 6. Overview of experimental procedure.

loaded with the pure DC signal direct from the Bitroide cycler and are therefore employed as the reference cells within this experiment. Cells 4–6, 7–9, 10–12 and 13–15 were electrically loaded using the same DC signal, but with the addition of an AC ripple component of magnitude: 10 Hz, 55 Hz, 254 Hz and 14.8 kHz respectively. As discussed in Section 3.1 the peak-to-peak magnitude of the current ripple was maintained constant at 1.2C. Each cell was exposed to 300 full charge–discharge cycles before being re-characterised using the procedures defined in Section 4.1. In total, each cell was exposed to 1200 full charge–discharge cycles and 4 re-characterisation tests at 300 cycles, 600 cycles, 900 cycles and 1200 cycles respectively.

#### 4.3. Ageing characterisation test

After each 300 cycle period, the cells were re-characterised using the same characterisation procedures noted in Section 4.1. After each characterisation, the new measured value of cell capacity was used to update the AC ripple test procedure with new values of peak current magnitude relative to the de-rated capacity (Section 3.2). This is to ensure that the cells are cycled within the safe operational limits defined by the manufacturer.

The total test duration for the experiment, including characterisation and cell cycling was in the order of 100 days.

## 5. Results

### 5.1. Capacity retention

The results for 1C capacity retention are summarised in Table 4. As it can be seen, there is a significant difference in the standard deviation of the measured capacity between cells cycled with and without the superposition of additional AC current ripple. With a pure DC cycle, the measured capacity of cells 1–3 are closely aligned with the average standard deviation from characterisation at 300, 400, 900 and 1200 cycles of 0.014 Ah and a maximum discrepancy of 0.04 Ah (i.e., 1.6% of the average capacity). However, for those cells electrically loaded with a coupled AC and DC signal, the standard deviation in their 1C capacity is much greater, with an average deviation of 0.052 Ah and a maximum discrepancy of 0.17 Ah (i.e., 7.3% of the average capacity). During testing, it is noteworthy that cell 6 (that was cycled using a 10 Hz AC signal) failed under re-characterisation at 300 cycles,

Table 4

Results of 1C capacity retention tests (the first column are the initial characterisation results). Note that after 300 cycles, cell 6 was found to be non-functional (cell voltage was approximately 2 volts) therefore it was not tested further and the associated data is not reported here.

Frequency	Cell	Cycle number				
		0	300	600	900	1200
0 Hz	Cell 1	2.86	2.58	2.53	2.36	2.42
	Cell 2	2.85	2.57	2.52	2.35	2.42
	Cell 3	2.82	2.55	2.50	2.32	2.40
	Std. dev.	0.0173	0.0129	0.0129	0.0173	0.01
10 Hz	Cell 4	2.79	2.64	2.54	2.47	2.35
	Cell 5	2.82	2.67	2.58	2.50	2.38
	Cell 6	–	–	–	–	–
	Std. dev.	0.0129	0.1190	0.1073	0.0616	0.0544
55 Hz	Cell 7	2.82	2.60	2.46	2.41	2.38
	Cell 8	2.82	2.69	2.55	2.49	2.45
	Cell 9	2.82	2.57	2.47	2.41	2.35
	Std. dev.	0.02	0.1212	0.0750	0.0383	0.0557
254 Hz	Cell 10	2.83	2.48	2.44	2.39	2.35
	Cell 11	2.81	2.43	2.44	2.35	2.30
	Cell 12	2.83	2.52	2.50	2.42	2.36
	Std. dev.	0.01	0.0367	0.0282	0.0289	0.0265
14.8 kHz	Cell 13	2.80	2.51	2.43	2.43	2.43
	Cell 14	2.83	2.39	2.33	2.34	2.28
	Cell 15	2.81	2.40	2.32	2.34	2.26
	Std. dev.	0.013	0.0545	0.0497	0.0424	0.076

since it was no longer able to accept a charge. Further work is ongoing to ascertain the cause of the cell failure through appropriate post-mortem analysis.

### 5.2. Pulse power test results

Examination of pulse power results indicate that, for the same SOC, the change in cell power density due to increasing the magnitude of pulse current is negligible. This implies that for this particular cell, diffusion limitation is not reached during the 10 s current pulse, (even at the maximum current rate). As with the capacity retention results, the primary observation, summarised in Table 5, is that a significant change in the spread of power density between DC only and the coupled AC–DC current waveform exist. Results show that the average standard deviation for DC cycling is only 0.006 kW/kg with a maximum discrepancy of 0.02 kW/kg (i.e.,

**Table 5**

Results of the pulse power tests, 10 s discharge power capability at 90% SOC; all values are in kW/kg (the first column are the initial characterisation results). A dash means the cells were not able to complete 10 s discharge pulse therefore data is not reported here.

Frequency	Cell	Cycle number				
		0	300	600	900	1200
0 Hz	Cell 1	1.247	1.173	1.148	1.067	1.125
	Cell 2	1.246	1.162	1.138	1.054	1.114
	Cell 3	1.244	1.153	1.135	1.048	1.114
	Std. dev.	0.001414	0.008185	0.005568	0.007958	0.005196
10 Hz	Cell 4	1.253	1.199	1.186	1.149	1.116
	Cell 5	1.249	1.198	1.186	1.154	1.125
	Cell 6	–	–	–	–	–
	Std. dev.	0.001633	0.000577	0	0.002082	0.003697
55 Hz	Cell 7	1.244	1.188	1.163	1.128	1.107
	Cell 8	1.247	1.198	1.175	1.142	1.125
	Cell 9	1.246	1.202	1.176	1.149	1.129
	Std. dev.	0.001414	0.005888	0.005916	0.008737	0.009592
254 Hz	Cell 10	1.249	1.139	1.133	0.000	1.091
	Cell 11	1.249	1.127	1.148	1.121	1.103
	Cell 12	1.253	1.171	1.151	1.126	1.104
	Std. dev.	0.001915	0.018574	0.007874	0.529627	0.005916
14.8 kHz	Cell 13	1.249	1.128	1.042	1.089	1.063
	Cell 14	1.250	1.159	1.119	1.101	–
	Cell 15	1.251	1.169	0.992	1.097	–
	Std. dev.	0.000816	0.017455	0.052237	0.005	0

1.8% of the average power density); the average standard deviation for cells subject to AC current ripple is approximately six times larger at 0.034 kW/kg with the maximum discrepancy being 0.127 kW/kg (i.e., 12% of the average power density). It is noteworthy that in addition to cell 6, cells 14 and 15 were unable to sustain an output voltage for the duration of the 10 s pulse at 90% SOC after 1200 cycles. Further work is ongoing to ascertain the cause of these cell failures through appropriate post-mortem analysis.

### 5.3. EIS results

Fig. 8 presents the impedance spectrums captured through EIS measurements taken during the initial characterisation tests performed on each cell. As it can be seen, there is very little difference between the different spectra for each cell before electrical loading commenced. EIS results presented in Fig. 9 indicate that in general,

cell degradation (measured via  $R_t$ ) is more severe for cells exercised with current ripple at higher frequencies. In the case of pure DC electrical loading, the EIS results presented in Fig. 7, indicate an increase in charge transfer resistance and a decrease of double layer capacitance. Table 6 provides the numerical results for  $R_t$  (a sum of ohmic resistance  $R_0$  and charge-transfer resistance  $R_{ct}$ ) for all 15 cells.

Fig. 9 presents EIS results after 600, 900 and 1200 cycles for a subset of cells in each frequency band: cell 1 (0 Hz), cell 47 (10 Hz), cell 7 (55 Hz), cell 10 (254 Hz) and cell 13 (14.8 kHz). The results indicate that at 254 Hz and 14.8 kHz there is an additional increase of both solid-electrolyte interphase (SEI) and double layer capacitance and decrease of charge transfer resistance compared with the case of pure DC cycling. Furthermore, in all cases, the results indicate that the total resistance ( $R_t - R_0$ ) increases as the frequency of the AC waveform increases towards

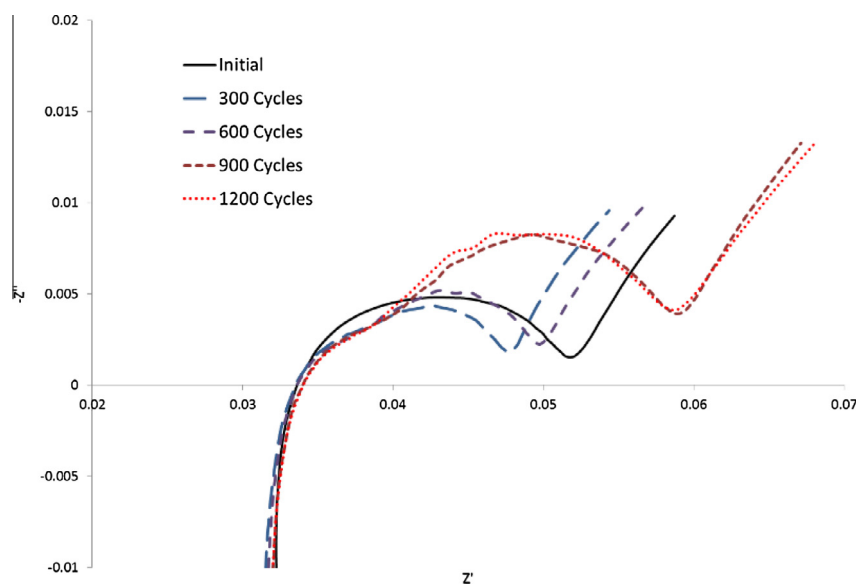


Fig. 7. EIS results for the reference cell (cell 1 – DC excitation only).

**Table 6**

Ohmic resistance ( $R_0$ ) and  $R_t$  (a sum of  $R_0$  and charge-transfer resistance  $R_{ct}$ ) from the EIS tests (the first column are the initial characterisation results). All values are in  $m\Omega$ . Cell 6 was found to be non-functional, therefore it was not tested further and the associated data is not reported here.

Frequency	Cell	0 Cycle		1200th Cycle	
		$R_{Ohmic}$	$R_t$	$R_{Ohmic}$	$R_t$
0 Hz	Cell 1	26.30	44.36	34.07	58.59
	Cell 2	26.34	44.16	34.56	60.12
	Cell 3	26.52	43.48	34.70	59.67
10 Hz	Cell 4	24.71	44.71	31.61	54.18
	Cell 5	23.29	44.61	29.69	52.33
	Cell 6	–	–	–	–
55 Hz	Cell 7	25.70	45.34	32.70	53.74
	Cell 8	24.68	45.19	29.83	52.67
	Cell 9	25.88	43.23	31.88	51.19
254 Hz	Cell 10	24.63	45.42	25.65	57.56
	Cell 11	25.00	45.60	24.17	55.67
	Cell 12	22.13	47.68	23.61	55.32
14.8 kHz	Cell 13	24.94	45.07	29.45	63.61
	Cell 14	24.33	45.37	29.21	57.36
	Cell 15	25.42	46.37	33.51	73.90

14.8 kHz. However, the rate of increase is not monotonically increasing with respect to frequency.

By comparing the EIS results presented in Figs. 8 and 9, it can be seen that cells cycled with a current ripple at 14.8 kHz, experience a relatively rapid rise in  $R_t$  (circa: 0.02 Ohms) between 0 and 600 cycles; the rate of rise of resistance ( $R_t$ ) for the same cells then reduces considerably between 600 and 1200 cycles. In contrast with other frequencies, cells cycled with a current ripple at 254 Hz show the formation of two clearly distinct semi-circles that is usually attributed to the formation or thickening of a film layer over the negative electrode [41]. While values of surface film resistance and charge transfer resistance are approximated by extrapolating the semi-circles to the  $Re(z)$  axis using an equivalent circuit model, the distinctness of the semi-circles may be interpreted as arising from electrode surface roughness [42]. The significance of this, including the underlying causality between the AC current excitation and the variations in the EIS results exhibited by each cell are not yet fully understood and is the subject of ongoing research within the University.

## 6. Discussions

### 6.1. Cell ageing

Capacity fade and power fade results, depicted in Figs. 10 and 11 respectively, along with EIS measurements suggest that the principle mechanism of degradation is the loss of cyclable lithium to thickening of the SEI layer. The growth of the SEI layer is widely attributed to cell operation at elevated temperatures [43]. The difference in cell surface temperature depicted in Fig. 12 for cells cycled with an AC–DC coupled load compared with the reference case (DC cycle only) shows a discrepancy no greater than 2 °C. Under thermal management, this surface temperature difference is completely suppressed.

In elucidating why cells under an AC–DC coupled load are relatively more degraded than under a DC load only, temperature effects cannot be dismissed. Even though the surface temperature of the cells was thermally managed to  $\pm 25$  °C, it is difficult to completely rule out temperature as an ageing factor due the possibility of internal temperature gradients forming, thus leading to larger SEI growth [44]. Since the value of cell impedance is a function of frequency, for a given current magnitude, different excitation frequencies will result in varying levels of heat generation. This may be attributed to the transference number for lithium ions being less than 1 at small timescales [45]. As a result, a portion of the anions will carry the current until the steady state diffusion gradient is established. At this point, the anions are in a state of equilibrium. However, in a system that is constantly being perturbed (with an AC ripple current), a state of equilibrium is never achieved.

### 6.2. Implications for the BMS control system

The results presented in Section 6 imply that the rate and magnitude of cell performance degradation is sensitive to variations in the frequency of the AC ripple current used to electrically load the cell. Cells exercised with an AC waveform of 14.8 kHz exhibit an increased level of capacity fade (circa: 2.4%) and a greater reduction in power fade (circa: 5%) when compared to the cells loaded with a pure DC signal for 1200 cycles. This is in general agreement with the EIS results presented in Fig. 9. However, it appears from these results that the rate of cell performance degradation is not

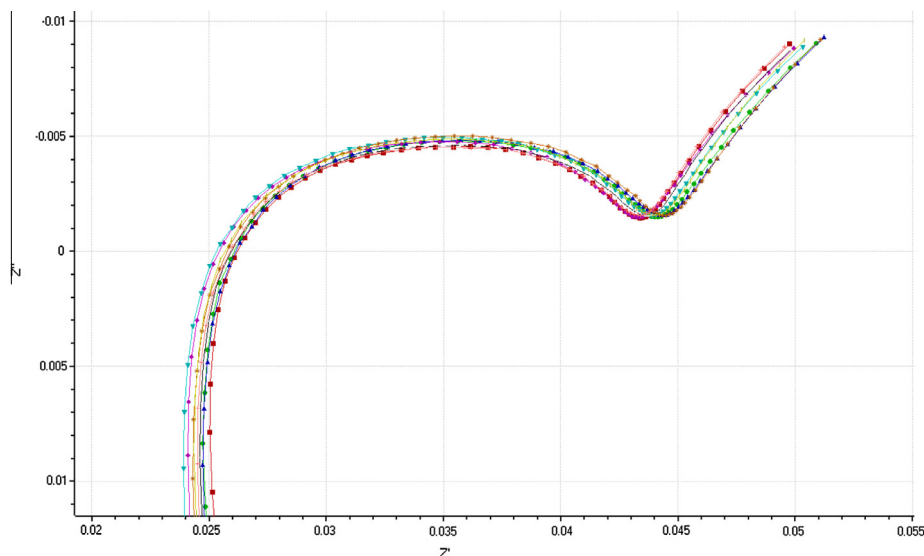
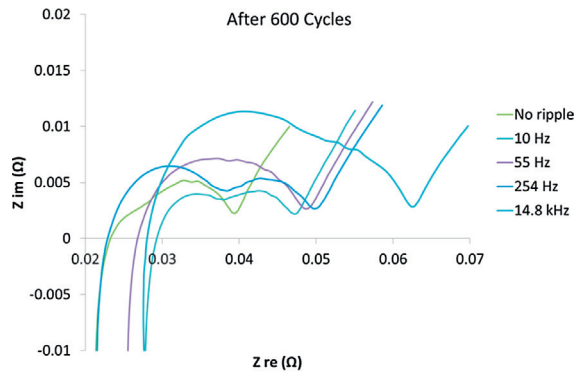
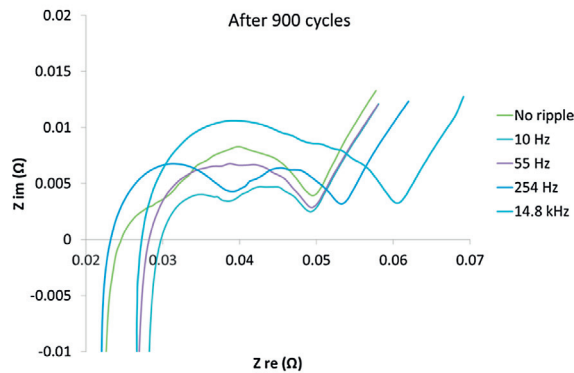


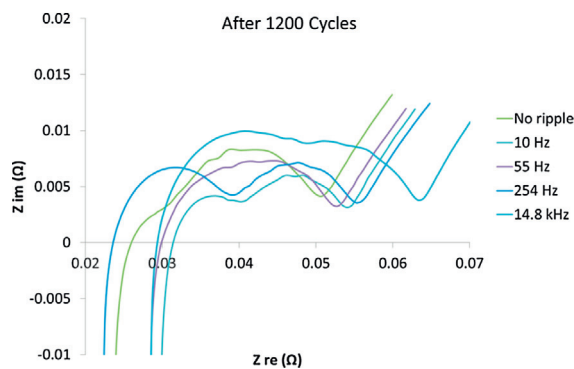
**Fig. 8.** Initial EIS results for all cells measured at 50% SOC.



(a) Cell impedance at 50 % SOC after 600 cycles for one cell for each test condition



(b) Cell impedance at 50 % SOC after 900 cycles for one cell for each test condition



(c) Cell impedance at 50% SOC after 1200 cycles for one cell for each test batch

**Fig. 9.** EIS results for cells at different frequencies: (a) after 600 cycles, (b) after 900 cycles and (c) after 1200 cycles.

linearly dependant on frequency. Irrespective of any absolute variations in cell ageing, arguably a more important observation is that all cells exercised with a component of AC current ripple experience a greater spread in both capacity fade and resistance rise. Managing this diversity may potentially drive further complexity in the systems engineering functions required to scale-up individual cells into a complete battery pack. A number of articles discuss the need to minimise cell-to-cell variations within the system as a mean to reduce the differential heat generation with the pack [46]. This challenge is particularly pertinent when cells are connected electrically parallel, when such variations can drive significant differences in current flow within adjacent parallel strings of the battery assembly [46]. The impact of AC ripple induced ageing may

therefore require increased levels of cell energy balancing and thermal management.

### 6.3. Further work

A number of opportunities exist where the research presented here may be further extended and refined. The results collected from this experimental study imply that the rate of cell degradation is not uniform and varies considerably with the inclusion of an AC waveform superimposed on a DC signal. However, given the limited dataset employed for this initial study, definitive conclusions regarding the underlying causality between the different ageing mechanisms cannot be made. The authors believe that these initial results warrant further research. Firstly, using novel cell imaging and autopsy methods, as discussed within [47] to better quantify the changes that occur within the material composition and structure of the cell post AC electrical loading. A better understanding of the underlying causality may also be achieved through the extension of electrochemical models, such as those described in [48] to study the possible causes such as temperature gradients internal to the cell (noted in Section 6.1). The second area of further work, is to reduce the potential impact of cell-to-cell variations by expanding the scope of the experimental study to encompass a greater number of cells of a given type. Expanding the experimental programme should also include using cells from a broader cross-section of manufacturers and chemistries. This will identify if the experimental results presented here are transferable to other cell technologies. Finally, given that the aim of this study was to assess the impact of varying frequency for the given AC current, further research should be undertaken to assess the relative degradation associated with varying the peak-peak amplitude of the AC current waveform in addition to the excitation frequency.

## 7. Conclusion

This paper documents an experimental investigation that studies the long-term impact of current ripple on battery performance degradation. A novel test environment has been designed to thermally manage the cells to 25 °C while simultaneously exciting the cells with a coupled DC and AC load profile that is representative of real-world vehicle use. Based on the impedance characteristics of the cell under test and a study into real-world data recorded from a HEV, five frequencies were highlighted for investigation: 10 Hz, 55 Hz, 254 Hz, 14.8 kHz and 0 Hz. The latter constituting the reference condition against which comparisons of relative ageing were made. Initial results highlight that both capacity fade and impedance rise increase as the frequency of the superimposed AC current increases. After 1200 full charge–discharge cycles, with a pure DC excitation, the measured capacity of the cells was found to be closely aligned with a standard deviation of 0.01 Ah and a maximum discrepancy of 0.02 Ah (i.e., 0.8% of the average capacity). However, for those cells electrically loaded with a coupled AC and DC signal, the standard deviation in their 1C capacity was observed to be much greater, having an average deviation of 0.076 Ah and a maximum discrepancy of 0.17 Ah (i.e., 7.3% of the average capacity). A similar divergence of cell properties was also observed with the power density of the aged cells after being cycled 1200 times. Cells exercised with a DC signal, the standard deviation was 0.005196 W/g. Conversely, for cells cycled with an AC ripple current of 14.8 kHz, the spread of values was found to be 10 times greater (circa: 0.052237 W/g after 600 cycles). This has important implications for the BMS control algorithms. Increased variations in cell capacity and impedance will cause differential current flows and heat generation within the battery pack

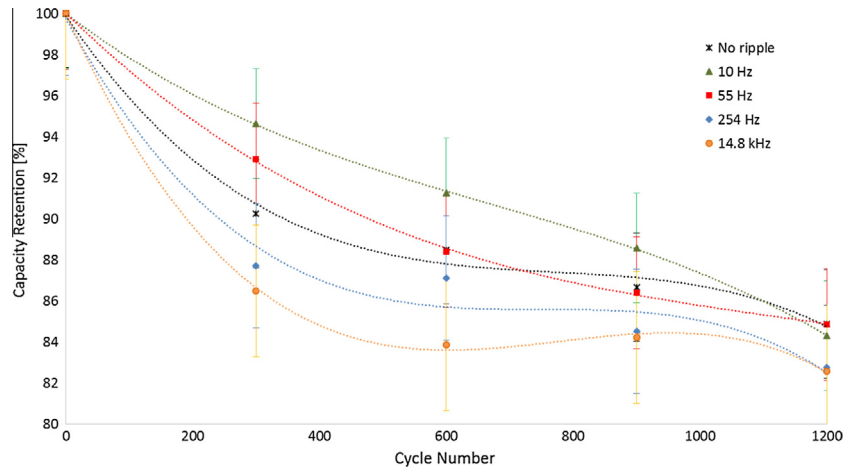


**Fig. 10.** Average capacity retention in percentage ( $\equiv 100 - \text{capacity fade}$ ) as a function of charge-discharge cycle number for different AC ripple frequencies. Dotted lines indicate polynomial 3rd order) lines of best fit with matching colours with markers. The capacity of each cell is normalised such that every cell is defined to have no capacity fade initially.

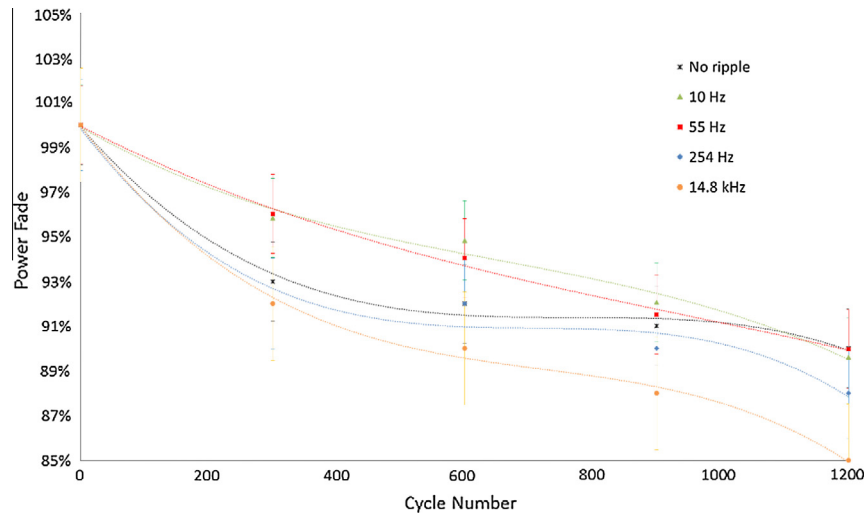


**Fig. 11.** Average power delivery capability in percentage ( $\equiv 100 - \text{power fade}$ ) as a function of charge-discharge cycle number for various AC ripple frequencies. Dotted lines indicate polynomial 3rd order) lines of best fit and have matching colours with markers. The capacity of each cell is normalised such that every cell is defined to have no capacity fade initially.

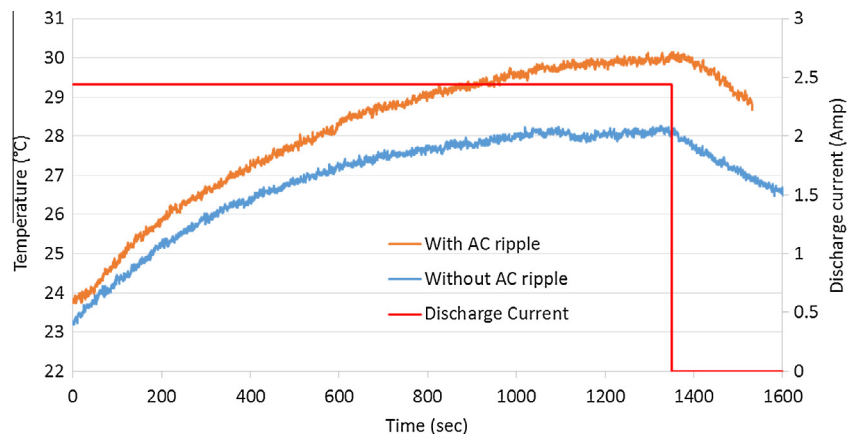


**Fig. 12.** The difference in temperature during discharge for cell 15 (cell exhibiting highest resistance rise after 1200 cycles) with and without AC ripple at 10 Hz). This test was carried out at ambient temperature without the cooling circuit after the final characterisation test was completed.



that if not properly managed will further reduce battery life and degrade the operation of the vehicle.

In conclusion, the experimental results presented highlight the potential for key electrical properties within the cell to diverge, over time, due to the inclusion of an AC excitation signal in addition to the traditional DC electrical loading. Unless this phenomenon is well understood at the design stage of the vehicle (e.g. during cell characterisation or technology selection) it may drive further complexity into design of the battery system. It is noteworthy that International Standards on battery cell characterisation methods, such as ISO and USABC [39,40] do not include tests to evaluate ageing under AC loading conditions. At this stage, the underlying causality between the frequency of the AC waveform and the rate of cell degradation is not fully understood. Defining these relationships is the focus of on-going research within the University. For example; by using novel cell imaging and autopsy methods to quantify changes in material composition and structure. Expanding the experimental programme to also include cells of different form-factor and chemistry will identify if the experimental results presented here are transferable to other cell technologies.

## Acknowledgments

This research was supported by the EPSRC (EP/M507143/1) and (EP/N001745/1), in collaboration with the WMG Centre High Value Manufacturing Catapult (funded by Innovate UK) in partnership with Jaguar Land Rover (JLR). The authors thank Dr. Gregory Offer (Imperial College London) and Dr. Gael Chouchelamane (JLR) for their contributions and efforts during the experimental activity and when post-processing the results.

## References

- [1] Berggren C, Magnusson T. Reducing automotive emissions—the potentials of combustion engine technologies and the power of policy. *Energy Policy* 2012;41:636–43.
- [2] Ou X, Yan X, Zhang X, Liu Z. Life-cycle analysis on energy consumption and GHG emission intensities of alternative vehicle fuels in China. *Appl Energy* 2012;90:218–24.
- [3] Wang H, Zhang X, Ouyang M. Energy consumption of electric vehicles based on real-world driving patterns: a case study of Beijing. *Appl Energy* 2015;157:710–9.
- [4] Kobayashi S, Plotkin S, Ribeiro SK. Energy efficiency technologies for road vehicles. *Energy Eff* 2009;2:125–37.
- [5] Tzeng G-H, Lin C-W, Opricovic S. Multi-criteria analysis of alternative-fuel buses for public transportation. *Energy Policy* 2005;33:1373–83.
- [6] Zapata C, Nieuwenhuis P. Exploring innovation in the automotive industry: new technologies for cleaner cars. *J Clean Prod* 2010;18:14–20.
- [7] Xu Y, Gbolagah FE, Lee D-Y, Liu H, Rodgers MO, Guensler RL. Assessment of alternative fuel and powertrain transit bus options using real-world operations data: life-cycle fuel and emissions modeling. *Appl Energy* 2015;154:143–59.
- [8] Lewis AM, Kelly JC, Keoleian GA. Vehicle lightweighting vs. electrification: life cycle energy and GHG emissions results for diverse powertrain vehicles. *Appl Energy* 2014;126:13–20.
- [9] Reitz RD, Duraisamy G. Review of high efficiency and clean reactivity controlled compression ignition (RCCI) combustion in internal combustion engines. *Prog Energy Combust Sci* 2015;46:12–71.
- [10] Chen F, Taylor N, Kringos N. Electrification of roads: opportunities and challenges. *Appl Energy* 2015;150:109–19.
- [11] Zhou Y, Wang M, Hao H, Johnson L, Wang H. Plug-in electric vehicle market penetration and incentives: a global review. *Mitig Adapt Strat Glob Change* 2014;20:777–95.
- [12] Juul N, Meibom P. Road transport and power system scenarios for Northern Europe in 2030. *Appl Energy* 2012;92:573–82.
- [13] Hutchinson T, Burgess S, Herrmann G. Current hybrid-electric powertrain architectures: applying empirical design data to life cycle assessment and whole-life cost analysis. *Appl Energy* 2014;119:314–29.
- [14] Erickson RW, Maksimovic D. Fundamentals of power electronics. Springer Science & Business Media; 2007.
- [15] Mi C, Peng FZ, Kelly KJ, O'Keefe M, Hassani V. Topology, design, analysis and thermal management of power electronics for hybrid electric vehicle applications. *Int J Electr Hybrid Veh* 2008;1:276–94.
- [16] Yilmaz M, Krein PT. Review of battery charger topologies, charging power levels, and infrastructure for plug-in electric and hybrid vehicles. *IEEE Trans Power Electron* 2013;28:2151–69.
- [17] Broussely M, Biensan P, Bonhomme F, Blanchard P, Herreyre S, Nechev K, et al. Main aging mechanisms in Li ion batteries. *J Power Sources* 2005;146:90–6.
- [18] Waag W, Käbitz S, Sauer DU. Experimental investigation of the lithium-ion battery impedance characteristic at various conditions and aging states and its influence on the application. *Appl Energy* 2013;102:885–97.
- [19] Ning G, Haran B, Popov BN. Capacity fade study of lithium-ion batteries cycled at high discharge rates. *J Power Sources* 2003;117:160–9.
- [20] Ouyang M, Feng X, Han X, Lu L, Li Z, He X. A dynamic capacity degradation model and its applications considering varying load for a large format Li-ion battery. *Appl Energy* 2016;165:48–59.
- [21] Nelson RF, Kepros MA. AC ripple effects on VRLA batteries in float applications. In: Battery conference on applications and advances, 1999. The fourteenth annual. IEEE; 1999. p. 281–9.
- [22] Enoki PRSAO. In: 5th ERA Seminar.
- [23] Vijayavalli R, Rao PV, Sampath S, Udupa H. Function of AC superimposed on DC in the anodic oxidation of lead in sulfuric acid. *J Electrochem Soc* 1963;110:1–4.
- [24] Okazaki S, Higuchi S, Nakamura O, Takahashi S. Influence of superimposed alternating current on capacity and cycle life for lead-acid batteries. *J Appl Electrochem* 1986;16:894–8.
- [25] Gerner SD, Ruhlmann TE, Dynasty Division, C&D Technologies 900 E. Keefe Ave Milwaukee, WI 53212.
- [26] Hosking D. Developments in lead/acid stationary batteries. *J Power Sources* 1993;45:111–7.
- [27] Catherino HA, BATTERIES | Alternating Currents A2 – Garche, Jürgen. In: Encyclopedia of Electrochemical Power Sources. Amsterdam: Elsevier; 2009. p. 489–98.
- [28] Uno M, Tanaka K. Influence of high-frequency charge-discharge cycling induced by cell voltage equalizers on the life performance of lithium-ion cells. *Vehicul Technol, IEEE Trans* on 2011;60:1505–15.
- [29] Smith K, Wang C-Y. Solid-state diffusion limitations on pulse operation of a lithium ion cell for hybrid electric vehicles. *J Power Sources* 2006;161:628–39.
- [30] Zhang J, Ge H, Li Z, Ding Z. Internal heating of lithium-ion batteries using alternating current based on the heat generation model in frequency domain. *J Power Sources* 2015;273:1030–7.
- [31] Capasso C, Veneri O. Experimental analysis on the performance of lithium based batteries for road full electric and hybrid vehicles. *Appl Energy* 2014;136:921–30.
- [32] Peterson SB, Apt J, Whitacre JF. Lithium-ion battery cell degradation resulting from realistic vehicle and vehicle-to-grid utilization. *J Power Sources* 2010;195:2385–92.
- [33] Zhang Y, Wang C-Y, Tang X. Cycling degradation of an automotive LiFePO4 lithium-ion battery. *J Power Sources* 2011;196:1513–20.
- [34] Perreault DJ, Afridi KK, Khan IA. Automotive applications of power electronics. In: Rashid MH, editor. The power electronics handbook. New York: Academic; 2001. p. 791–813.
- [35] Welch PD. The use of fast Fourier transform for the estimation of power spectra: a method based on time averaging over short, modified periodograms. *IEEE Trans Audio Electroacoust* 1967;15(2):70–3.
- [36] Stoica P, Moses R. Spectral analysis of signals. Prentice Hall; 2005.
- [37] Lu L, Han X, Li J, Hua J, Ouyang M. A review on the key issues for lithium-ion battery management in electric vehicles. *J Power Sources* 2013;226:272–88.
- [38] Barai A, Widanage WD, Marco J, McGordon A, Jennings P. A study of the open circuit voltage characterization technique and hysteresis assessment of lithium-ion cells. *J Power Sources* 2015;295:99–107.
- [39] ISO. Electrically propelled road vehicles – test specification for lithium-ion traction battery packs and systems. In: Part 1: High-power applications. Geneva, Switzerland: International Organization for Standardization; 2011.
- [40] U.S.D.O. Energy, Battery Test Manual for Plug In Hybrid Electric Vehicles. In: V. T.P. Energy Efficiency and Renewable Energy, editor, Idaho Operations Office; 2014.
- [41] Zhang SS, Xu K, Jow TR. EIS study on the formation of solid electrolyte interface in Li-ion battery. *Electrochim Acta* 2006;51:1636–40.
- [42] Franklin AD. Electrode effects in the measurement of ionic conductivity. *J Am Ceram Soc* 1975;58:465–73.
- [43] Vetter J, Novák P, Wagner MR, Veit C, Möller KC, Besenhard JO, et al. Ageing mechanisms in lithium-ion batteries. *J Power Sources* 2005;147:269–81.
- [44] Troxler Y, Wu B, Marinescu M, Yufit V, Patel Y, Marquis AJ, et al. The effect of thermal gradients on the performance of lithium-ion batteries. *J Power Sources* 2014;247:1018–25.
- [45] Xiao M, Choe S-Y. Impedance model of lithium ion polymer battery considering temperature effects based on electrochemical principle: Part I for high frequency. *J Power Sources* 2015;277:403–15.
- [46] Bruen T, Marco J. Modelling and experimental evaluation of parallel connected lithium ion cells for an electric vehicle battery system. *J Power Sources* 2016;310:91–101.
- [47] Somerville L, Jennings P, McGordon A, Lyness C, Prezas P, Basco J, Barenó J, Duong T, Bloom I. Effects of fast charging on lithium-ion cells, Meeting Abstracts, MA2015-01; 2015. p. 461–461.
- [48] Wang H, Varghese J, Pilon L. Simulation of electric double layer capacitors with mesoporous electrodes: effects of morphology and electrolyte permittivity. *Electrochim Acta* 2011;56:6189–97.